Understanding Oxygen Activation on Metal- and Nitrogen-Codoped Carbon Catalysts

Eisenberg, D.; Slot, T.K.; Rothenberg, G.

DOI
10.1021/acscatal.8b01045

Publication date
2018

Document Version
Final published version

Published in
ACS Catalysis

ACS Catalysis

Research Article

Cite This: ACS Catal. 2018, 8, 8618–8629

pubs.acs.org/acscatalysis

Understanding Oxygen Activation on Metal- and Nitrogen-Codoped Carbon Catalysts

David Eisenberg,*[,§] Thierry K. Slot,[‡] and Gadi Rothenberg[‡]

[§]Schulich Faculty of Chemistry and the Grand Technion Energy Program, Technion—Israel Institute of Technology, Haifa 3200003, Israel

[‡]Van 't Hoff Institute for Molecular Sciences, University of Amsterdam, Science Park 904, Amsterdam 1098 XH, The Netherlands

Supporting Information

ABSTRACT: Multidoped carbons are often used for oxygen activation catalysis, both in heterogeneous catalysis and electrocatalysis. Identifying their catalytic sites is crucial for developing better catalysts. We now report an in-depth study into O_2 activation on an important class of materials: carbons codoped by nitrogen and 10 different metals (V, Cr, Mn, Fe, Co, Ni, Cu, Zn, Mo, and Pb). To identify catalytic sites, we studied their composition and structure (both bulk and surface) by a wide range of techniques, including temperature-programmed reduction, X-ray diffraction, electron microscopy, X-ray photoelectron spectroscopy, and N_2 sorption porosimetry. The O_2 activation step was studied by electrochemical oxygen reduction. To assign active sites, the electrocatalytic activity, selectivity, and stability were correlated to material composition and to known reactivity pathways. Two types of sites for O_2 activation were identified and assigned for each multidoped material: (1) particles of partially reduced metal oxides and (2) metal−nitrogen clusters embedded into the carbon matrix. The detailed assignment correlates to activity in alcohol oxidation through similar volcano plots and leads to practical suggestions for catalyst development.

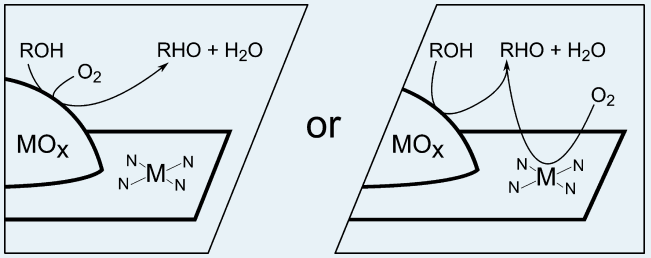

KEYWORDS: *carbon-based catalysts, tandem catalysis, oxygen activation, metal oxides, active site, oxygen reduction reaction, temperature-programmed reduction, cooperative catalysis*

INTRODUCTION

Carbons codoped with both metallic and nonmetallic elements are promising heterogeneous catalysts for aerobic oxidation reactions.[1−6] Nonmetallic elements such as N, P, or B are typically embedded in the graphite surface, while the metal dopants may appear as inorganic particles and/or coordinated to heteroatoms. Such carbons are also used in batteries,[7,8] in supercapacitors[9,10] and as electrocatalysts for the oxygen reduction reaction (ORR) in fuel cells.[11−15]

Interestingly, both in heterogeneous catalysis and electrocatalysis applications, multidoped carbons are often used to activate molecular oxygen.[1−6] O_2 activation is an important yet challenging reaction: the O═O bond energy is high (498 kJ/mol), and the molecule is kinetically stabilized by its triplet electronic configuration. Activating molecular oxygen depends on understanding what are the catalytic sites and how they operate.

To design multidoped carbons rationally, we must first establish reliable synthesis/structure links. The problem is that many carbons are made by complex pyrolysis reactions of diverse organic matter. Predicting and directing the evolution of their composition (sp^2/sp^3 ratio and doping) and structure (porosity, crystallinity, and domain sizes) is difficult.[16] Metal ions in the precursors complicate things even further. Iron and nickel, for example, catalyze the growth of carbon nanotubes,[17,18] whereas molybdenum tends to form carbides[19] and alkali-earth metals form carbonates.[20,21] Doping a carbon also changes its wettability, conductivity, and work function.[22−24]

The second challenge in using multidoped carbons for oxygen activation lies in understanding the structure−activity correlations. The catalytic sites can range from single-atom sites, such as edge-positioned nitrogen atoms[25] or carbon-embedded Fe−N_4 complexes,[26] to large inorganic particles.[15] Much research is devoted to determining active site structure and linking it to catalytic activity.

Recently, we reported that carbons codoped by nitrogen and metallic elements can catalyze the oxidation of alcohols[4] and alkenes.[6] In these catalysts, as well as in others in the literature, the role of each dopant remains unclear.[1−3,27−29] Does alcohol oxidation happen solely on the metal oxide (MO_x) particles (Figure 1a), or is this an example of tandem catalysis, with MO_x particles binding the substrate and surface-embedded M−N_x clusters activating the oxygen (Figure 1b)?

Here we identify the catalytic sites for O_2 activation on these multidoped carbons. Starting with N-doped carbon as our active support, we dope it with 10 metals (V, Cr, Mn, Fe, Co,

Received: March 15, 2018
Revised: July 26, 2018
Published: August 6, 2018

DOI: 10.1021/acscatal.8b01045
ACS Catal. 2018, 8, 8618−8629

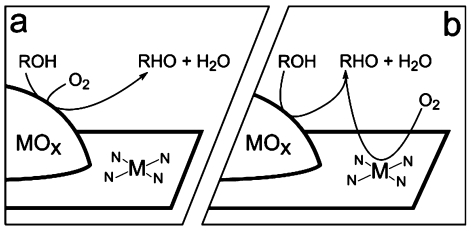

Figure 1. Two scenarios for alcohol oxidation reaction on M−N−C materials: (a) catalysis on the MO_x particles, (b) tandem catalysis, with alcohol oxidation on the MO_x particle and O_2 activation on a surface-embedded M−N_x cluster.

Ni, Cu, Zn, Mo, and Pb). We then examine the composition, structure, and bonding in these catalysts, using both bulk and surface techniques. To understand the O_2 activation step in catalytic oxidations, we study the electrocatalytic oxygen reduction reaction (ORR). The active sites for O_2 activation in catalytic and electrocatalytic reactions are similar, sharing peroxide and hydroxide surface-localized intermediates.[30−33] Thus, the electrocatalytic activity, selectivity, and stability of the M−N−C materials help us to identify the oxygen activation sites.

EXPERIMENTAL SECTION

Synthesis of Multidoped Carbons.[34,35] Magnesium nitrilotriacetate ($MgNH(CH_2COO)_3(H_2O)_3$) was prepared from a solution of basic magnesium carbonate and nitrilotriacetic acid at 85 °C, precipitated by ethanol, and dried. The powder was pyrolyzed in quartz boats under argon flow (900 °C/1 h, ramp rate 10 °C/min), yielding a nitrogen-doped carbon loaded with MgO nanoparticles. The MgO was washed out by overnight stirring in 1 M HCl, followed by washing with 5 L of deionized (DI) water, overnight drying at 70 °C, and a final annealing in argon (1000 °C/1 h, ramp rate 5 °C/min). The resulting N-doped, hierarchically porous carbon (100 mg) was impregnated with metal salts (0.2 mL, 0.66 M).[4] The salts included NH_4VO_3 (with 2 equiv of oxalic acid for dissolution), $Cr(NO_3)_3{\cdot}9H_2O$, $Mn(NO_3)_2{\cdot}4H_2O$, $Fe(NO_3)_3{\cdot}9H_2O$, $Co(NO_3)_2{\cdot}6H_2O$, $Ni(NO_3)_2{\cdot}6H_2O$, $Cu(NO_3)_2{\cdot}3H_2O$, $Zn(NO_3)_2{\cdot}6H_2O$, $(NH_4)_6Mo_7O_{24}{\cdot}4H_2O$, and $Pb(NO_3)_2$. The powder was then dried at 75 °C overnight and annealed in argon (300 °C/1 h), to yield the final M−N−C material. Chemicals were obtained from commercial sources (>99% pure) and used as received.

Material Characterization. Scanning electron microscopy (SEM) was done on a Zeiss EVO50 microscope operated at 15 kV. Temperature-programmed reduction was performed by placing 25 mg of sample sandwiched between two quartz wool plugs in a quartz tube reactor (4 mm inner diameter), purging with N_2, and applying a flow of 5% H_2/N_2. The system was allowed to equilibrate and then heated at 5 °C/min to 800 °C (no hold time). X-ray diffraction (XRD) patterns were obtained with a MiniFlex II diffractometer using Ni-filtered Cu Kα radiation, at 30 kV and 15 mA. X-ray photoelectron spectroscopy (XPS) measurements were carried out using a PHI VersaProbe II scanning XPS microprobe (Physical Instruments AG, Germany), using a monochromatic Al Kα X-ray source of 24.8 W power with a beam size of 100 μm. The spherical capacitor analyzer was set at a 45° takeoff angle with respect to the sample surface. The pass energy was 46.95 eV, yielding a full width at half-maximum of 0.91 eV for the Ag $3d_{5/2}$ peak. Peaks were calibrated using the C 1s position. Curve fitting was done using XPSPeak 4.1. N_2 adsorption−desorption isotherms were measured on a Thermo Scientific Surfer instrument at 77 K, using vacuum-dried samples (200 °C/3 h). Isotherms were analyzed by the ThermoFischer Advanced Data Processing 6.0 software, using the two-parameter Brunauer−Emmett−Teller (BET2) model for specific surface area.

Electrochemistry. Inks of the catalytic powders were prepared according to the following proportions: 0.80 mL of DI water, 0.20 mL of ethanol, 10 μL of Nafion (5 wt % in water/isopropanol), and 1 mg of M−N−C powder. Inks were sonicated, stirred, and dropcast on a glassy carbon working electrode (ϕ = 5 mm, A = 0.196 cm^2) to give a total catalyst loading of 30 μg, or 153 $\mu g/cm^2$. Electrochemical experiments were performed in a three-electrode homemade glass cell, filled with KOH (0.1 M, 150 mL), and stabilized at 25.0 ± 0.1 °C. A Gamry Reference 600 potentiostat was employed, together with a Gamry RDE710 rotating electrode setup. A saturated calomel electrode (SCE) separated from the solution by a 10 cm bridge was used as a reference electrode, and a graphite rod was used as a counter electrode. Potentials were reported vs reversible hydrogen electrode (RHE) by adding 1.011 for pH 13. Nitrogen (99.999%) or oxygen (99.999%) were bubbled for 30 min to saturate the solution and were flowed above the solution during the experiments. Cyclic voltammetry experiments were performed in O_2-saturated 0.1 M KOH solution and corrected for background currents in a N_2-saturated solution (Figure 7a). The number of electrons transferred per O_2 molecule (n) was calculated by Koutecký−Levich analysis from linear sweep voltammetry curves performed on a rotating disk at rotation speeds of 400−2400 rpm. To compare stability, chronoamperometry experiments recorded the decay of the ORR activity under continuous operation (E = 0.41 V vs RHE), while bubbling oxygen and stirring.

RESULTS AND DISCUSSION

We prepared the carbon support following published procedures, based on pyrolysis of a Mg-based metal−organic framework.[34−36] These carbons have a high surface area (1570 m^2/gr) and high nitrogen content (5.9 at % by XPS). They feature interconnected micro-, meso-, and macropores, assisting mass transport. A percolating network of graphitic shells boosts the electrical conductivity of the matrix and charge transfer between redox sites. The carbons were loaded with 1.3 mmol/g of metal solutions by incipient wetness vacuum impregnation. A reductive heat treatment (300 °C/1 h) under argon yielded the final M−N−C materials, containing 0.8−2.3 at % of metals (Table 1). Unlike copyrolysis,[3] this strategy fixes the carbon matrix, allowing for a fair comparison between the metals.

Scanning Electron Microscopy. Scanning electron microscopy (SEM, Figure 2) reveals highly similar MO_x particles for all metals, as expected from incipient wetness impregnation.[37] The particles are spherical or near-spherical, between 100−400 nm in diameter. Further analysis of the subsurface by backscattered electrons (see Figure S1 in the Supporting Information) reveals many more particles under the carbon surface, suggesting a firm embedding in the carbon support. Thus, combining incipient wetness impregnation with mild reduction yields structurally similar materials, allowing us to focus on the finer distinctions between the metals.

Temperature-Programmed Reduction. Temperature-programmed reduction (TPR) in a flow of 5% H_2 in N_2 was

DOI: 10.1021/acscatal.8b01045
ACS Catal. 2018, 8, 8618−8629

Table 1. Composition of Metal- (M) and Nitrogen-Codoped Carbons

M	metal content[a] (at %)	MO_x particle diameters[b] (nm)	MO_x composition, crystalline phases underlined[c]	M−N binding[d]
V	1.12	200−400	V_2O_5, VO_2	some
Cr	0.84	100−300	Cr_2O_3, CrO_3	significant
Mn	2.32	200−500	Mn_3O_4, MnO_2, Mn_5O_8, Mn_2O_3	some
Fe	1.11	200−300	Fe_2O_3, Fe_3O_4	significant
Co	1.38	200−300	CoO, Co_3O_4	significant
Ni	1.25	200−300	NiO, NiOOH	significant
Cu	1.82	200−300	CuO, Cu_2O	significant
Zn	2.22	100−300	ZnO	some
Mo	1.53	200−300	MoO_3	significant
Pb	2.34	100−400	PbO	none

[a]From X-ray photoelectron spectroscopy (XPS) integration. [b]From scanning electron microscopy (SEM). [c]From temperature-programmed reduction (TPR), X-ray diffraction (XRD), and XPS. Crystalline phases are underlined; the rest are amorphous. [d]From XPS in the N 1s region.

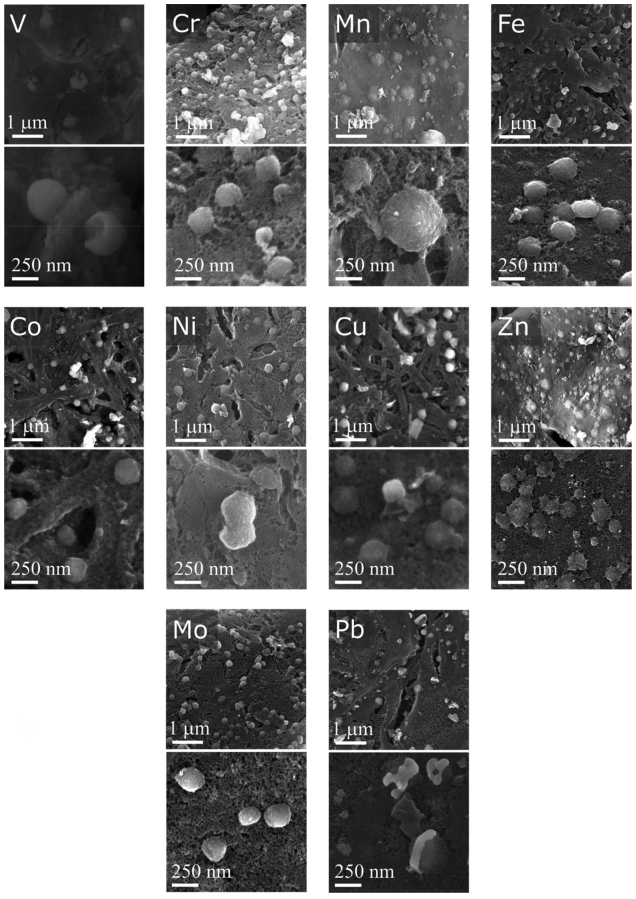

Figure 2. Scanning electron micrographs of the M−N−C samples. Each element is represented by low- and high-magnification micrographs.

used to identify the metal oxidation states and describe particle−surface interactions (Figure 3). Assigning TPR peaks is complicated when the same oxidation state is present in different crystals or interacts strongly with the support surface. Moreover, extrinsic factors such as metal loading, particle size, or heating rates may also shift the reduction temperatures.[38] In our case, the homogeneity of the MO_x particles suppresses the effects of particle size and loading, facilitating comparison by TPR.

All TPR traces show a support gasification reaction above 600 °C (Figure 3, denoted by "X"). This is the metal-catalyzed carbon methanation reaction ($C + H_2 \rightarrow CH_4$).[39,40] The Cr−N−C trace is typical for mixed Cr(III)−Cr(VI) oxides.[41−43] The main peak at 450 °C (2) corresponds to the reduction of Cr(VI) to Cr(III). Cr(VI) chromates with different degrees of oligomerization are found on large Cr_2O_3 particles.[41,43] The TPR shoulder at 380 °C (1) is attributed to support interactions and/or crystallization of such surface Cr(VI) species.[41] Peak 3 corresponds to further reduction of the Cr_2O_3 particles to CrO.[42] The Mn−N−C trace exhibits multiple peaks, typically assigned to oxides such as MnO_2, Mn_5O_8, and possibly Mn_2O_3 and Mn_3O_4. The lower-temperature peaks (250−400 °C, peaks 1 and 2) may reflect the reduction of Mn(IV),[44,45] Mn(IV/III),[44] and possibly Mn(III).[44] Peak 3 corresponds to reduction of either Mn(III)[46] or carbon-stabilized MnOx species.[47] Higher-temperature peaks (4 and 5) may be assigned to the reduction of Mn(II/III),[44,47] bulk Mn(IV),[46] or surface-interacting MnO_x species.[47] Finally, MnO_x catalyzes methanation, lowering its temperature by ∼100 °C relative to free-standing activated carbon.[47] The Fe−N−C trace shows Fe_2O_3 reduced to Fe_3O_4 (350 °C, 1), then to FeO (450 °C, 2), and finally to Fe (610 °C, 3).[48−51] The low-temperature shoulder in peak 1 reveals some Fe_3O_4 in the starting sample.[48] Peak 4 may be assigned to reduction of micropore-confined FeO_x particles[50] or to support gasification.[51,52] The broadening of peaks 2 and 3 may indicate particle−support interactions.[48,50] Similarly, Co_3O_4 is first reduced to CoO (360 °C, 1) and then to metallic cobalt (460 °C, 2).[53,54] The high intensity of the second peak shows that both are present in the sample. Reductions above 400 °C reflect carbon methanation combined with particle−support interactions.[39,53] For Ni−N−C, we see two types of NiO: large particles with little support interaction (400 °C, 1)[55−57] and smaller, harder-to-reduce particles (520 °C, 2). Peak 2 is assigned to pore-constrained[55,56] or support-stabilized[55,58,59] NiO. A shoulder below 350 °C suggests a higher oxidation state, either Ni_2O_3 or NiOOH.[55] In the Cu−N−C trace, CuO is reduced to Cu_2O (280 °C, 1) and then to metallic copper (380 °C, 2).[40,60] The splitting in peak 1 indicates weakly and strongly interacting CuO particles. The Zn−N−C trace identifies only well-dispersed ZnO (reduction at 400 °C).[61,62] For Mo−N−C, the first two peaks correspond to the reduction of MoO_3 to MoO_2.[38,58,63] The difference is attributed to octahedral/tetrahedral Mo(VI) species and/or to support interactions of the MoO_3.[63] Peak 3 (650 °C) is assigned to Mo(IV) → Mo(II) reduction, with the latter either an oxide or a carbide.[64] Finally, the H_2-TPR traces of Pb−N−C and V−N−C are harder to assign. In both, the typical oxides (PbO and V_2O_5, respectively) are reduced above 600 °C when present as bulk powder,[65−67] and support interactions lower reduction temperatures to 400 °C.[67−69] Peak 1 in the VO_x trace probably belongs to V_2O_5 with strong interactions to the support.[70−72] Peak 3 in the PbO_x trace is probably bulk PbO, with the early peaks (1 and 2) relating to support interactions or to unreduced $Pb(NO_3)_2$.[61]

Overall, the H_2-TPR describes several oxides (mostly partially reduced), with significant particle−support interactions. The reducing species may be the carbon itself or volatile

DOI: 10.1021/acscatal.8b01045
ACS Catal. 2018, 8, 8618−8629

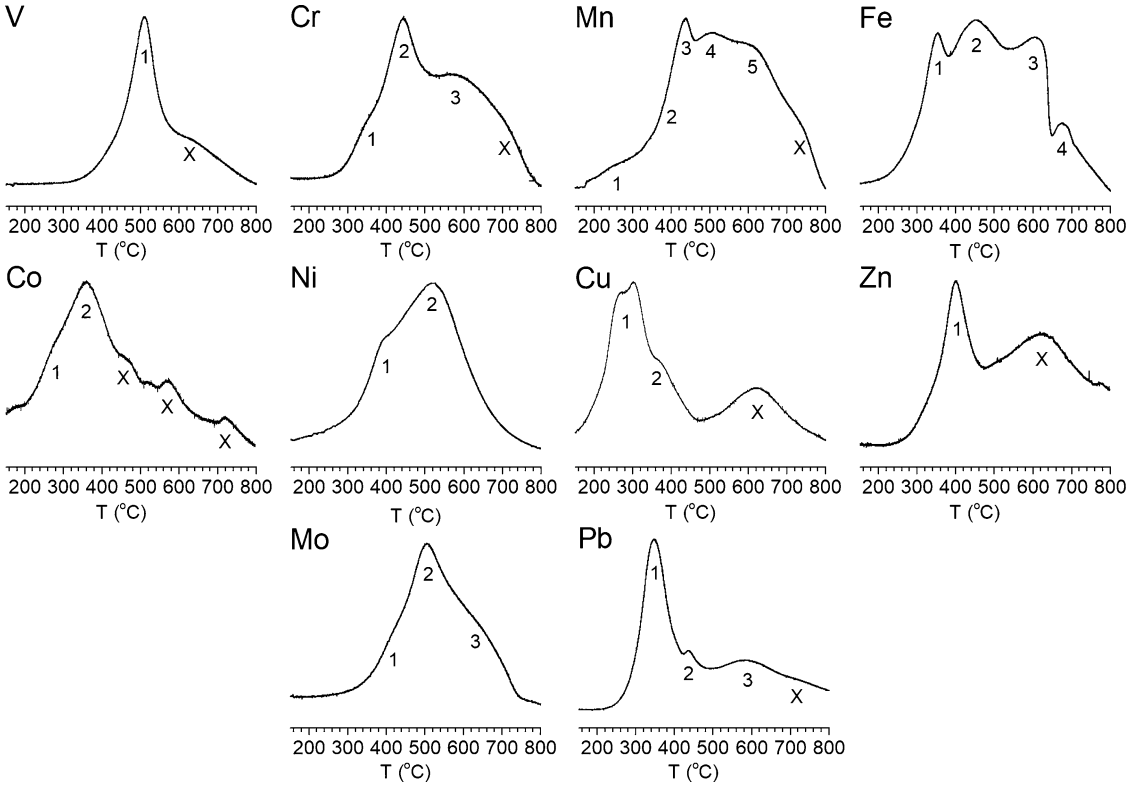

Figure 3. H_2-TPR plots of the 10 M−N−C samples. Signal intensity corresponds to H_2 consumption (arbitrary units, normalized). The number-marked peaks correspond to reductions of the metal ion (see text for assignment), and X denotes gasification (methanation) of the carbon support.

species released from it during the annealing step. Indeed, the annealing temperature (300 °C) is close to the temperature at which carbon methanation may begin, especially when catalyzed by metals. The "support-interacting" species could be particles, clusters, or even strongly bound metal atoms.

X-ray Diffraction. X-ray diffraction (XRD) showed that most MO_x particles are amorphous (Figure S2). Only the Mn-, Cu-, and Zn−N−C samples displayed additional diffraction peaks (Figure 4), corresponding to Mn_3O_4, CuO, and ZnO

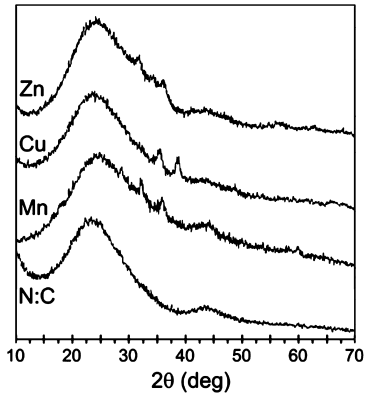

Figure 4. X-ray diffractograms of four M−N−C samples.

(JCPDS cards 01-080-0382, 48-1548, and 89-1397, respectively). Importantly, the presence of crystalline phases does not rule out additional, amorphous phases in the catalysts—for example, the lower reduction states of Mn that were suggested by TPR.

X-ray Photoelectron Spectroscopy. X-ray photoelectron spectroscopy (XPS) was used to describe composition and bonding on the surface of both MO_x particles and the N:C support (Figures 5 and S3; see Supporting Information for deconvolution method). The pristine N-doped carbon contains pyridinic (398.3 eV), pyrrolic (399.5 eV), graphitic (400.9 eV), and oxidized (402.9 eV) nitrogen atoms.[73] Pyridinic nitrogens are suitable for metal coordination,[74] and 300 °C is sufficient temperature for forming metal−nitrogen bonds.[75] XPS in the N 1s region is more useful for detecting metal−nitrogen bonding than metal XPS, which often has low sensitivity due to symmetry breaking and charge redistribution related to the binding. Indeed, the spectra reveal that metal codoping shifts the N 1s binding energies. Introducing the metal leads to a peak in the intermediate region (398.5−400 eV) in most materials, suggesting the formation of new metal−nitrogen bonds.[2,11,24,28,74−80] Other possible assignments for this new peak could be pyrrolic or pyrimidonic nitrogen. These moieties, however, are unlikely to form as a result of an impregnation with metal and mild heat treatment. The new M−N bonds vary in intensity between the cations and are most obvious for Cr-, Fe-, Co-, Ni-, and Cu-based carbons (Figure 5). The $M-N_x$ clusters are dispersed on the carbon surface, in addition to the MO_x particles. Alternative methods were considered to confirm metal−nitrogen binding, namely, Fe−Mössbauer and X-ray absorption spectroscopies. These methods, however, are unsuitable in the current composites, due to the small percentage of metals in $M-N_x$ clusters (most of it is in the oxides) and the similarity in X-ray absorption between M−N and M−O bonds.

In the metal regions of the XPS (Figure 6), most spectra are too complex for reliable mathematical deconvolution, especially when the signal-to-noise ratio is low and varies between samples. Nevertheless, "shape fitting" (overlaying the spectra with literature spectra) helped identify oxidation states

DOI: 10.1021/acscatal.8b01045
ACS Catal. 2018, 8, 8618−8629

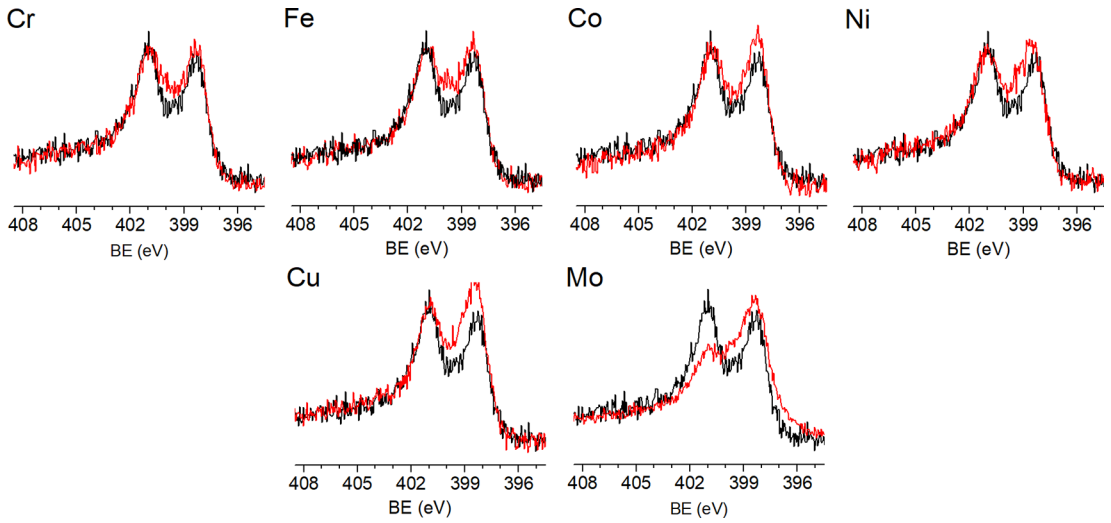

Figure 5. XPS in the N 1s region of the metal-free N-doped carbon (black trace) and the corresponding M−N−C composites (red traces).

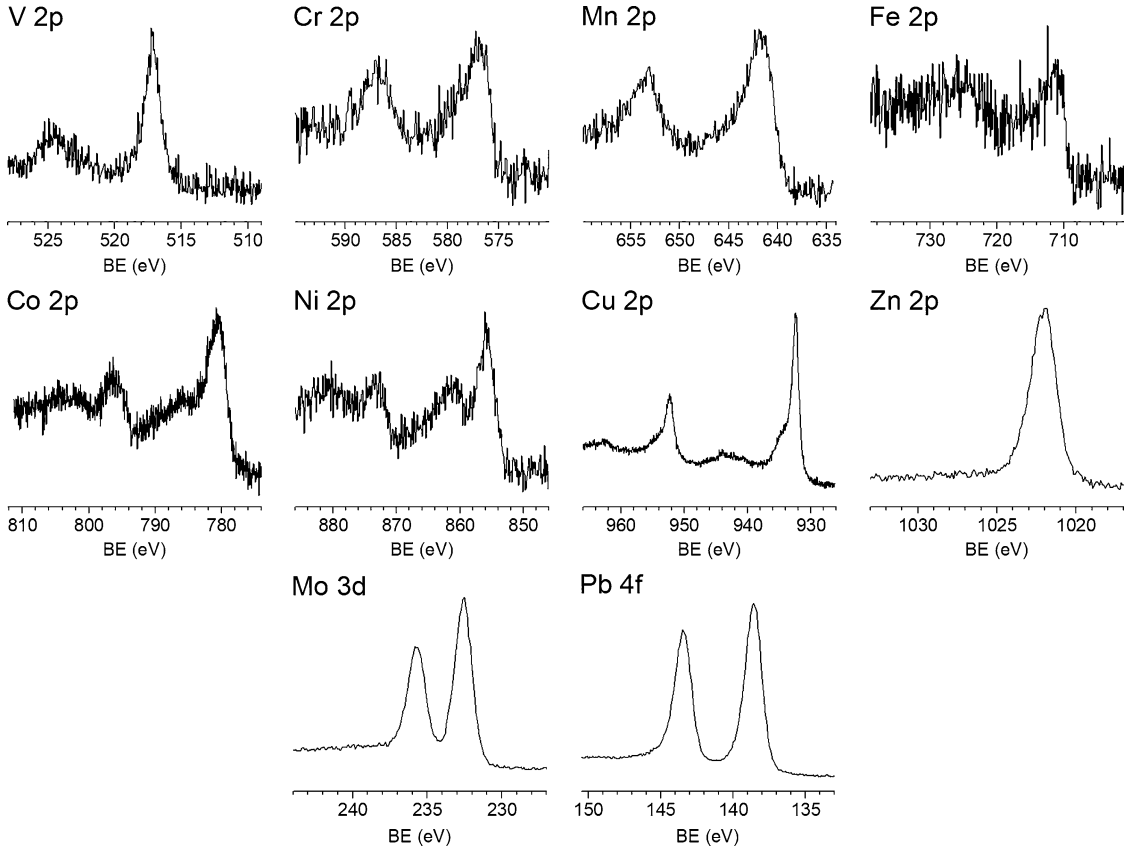

Figure 6. XPS of the M−N−C samples in the metal regions.

and binding modes on the surfaces of MO_x particles. This method helps avoid overfitting of broad peaks and focuses on peak positions and relative magnitudes. The V 2p XPS is characteristic to V_2O_5, based on the high-energy binding energy of the $2p_{3/2}$ peak (517.2 eV).[81,82] Shape fitting shows that there might also be traces of VO_2, indicating partial reduction of V(V) to V(IV).[81] In the Cr 2p XPS, two doublets ($2p_{3/2}$ peaks at 576.6 and 579.2 eV) indicate the presence of Cr(III), either as Cr_2O_3 particles or as Cr−N_4 sites. Both have typical binding energies of 576.5−576.7 eV.[43,83−85] In addition, Cr(VI) is present, probably as a CrO_3 layer on the surface of Cr_2O_3 particles.[43,83] Shape and position comparison of the Mn 2p XPS reveals Mn(III) and Mn(IV) oxidation states.[86−88] These probably correspond to the Mn_2O_3 and MnO_2 phases detected earlier by TPR, rather than to Mn−N centers (which are scarce, according to N 1s XPS). In the Fe XPS spectrum, a typical $2p_{3/2}$ peak of Fe(III) appears at 710.4 eV,[83] with some contribution from Fe(II). These oxidation states may be related to Fe_2O_3 with some residual FeO and/or to Fe^{III}−N_4 clusters embedded into and interacting with the carbon sheets.[89] The Co 2p XPS signals indicate a mixture of Co(II) and Co(III) states.[90−92] These ions could be located in

DOI: 10.1021/acscatal.8b01045
ACS Catal. 2018, 8, 8618−8629

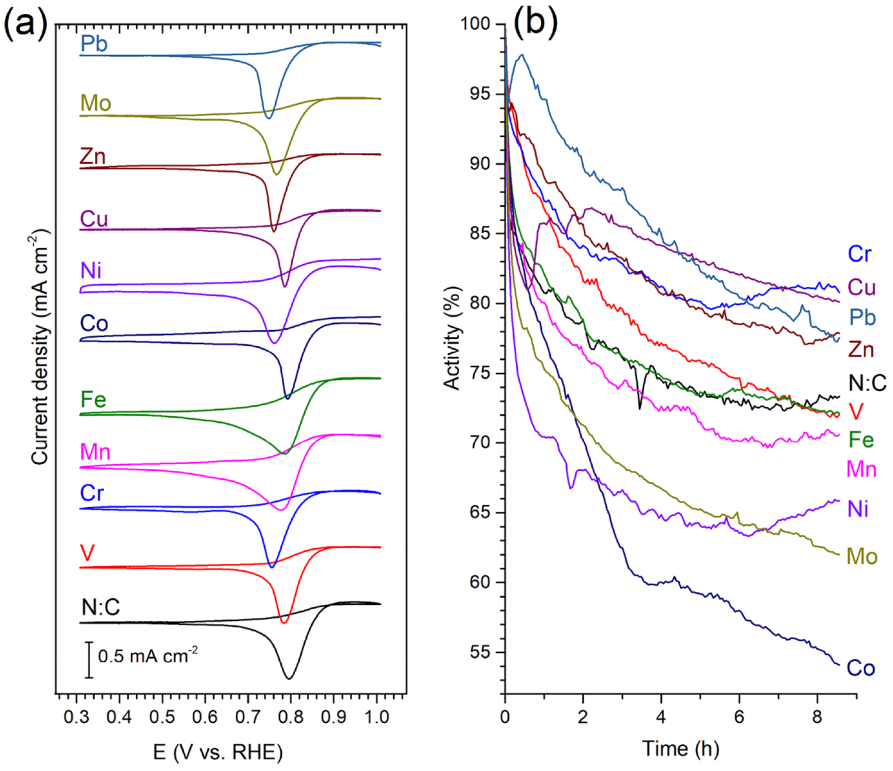

Figure 7. Electrocatalytic ORR over M−N−C samples. (a) Cyclic voltammograms in an O_2-saturated 0.1 M KOH solution, scan rate 10 mV/s, after subtraction of the current in a N_2-saturated solution and normalization relative to the peak current of the pristine carbon. (b) Decay of ORR current over time, operating at 0.4 V vs RHE under continuous O_2 bubbling and stirring.

the Co_3O_4 particles detected by TPR, to partially reduced (CoO) or oxidized (Co_2O_3) oxides, or to Co−N_x centers.[93] Similarly, the Ni 2p XPS shows signals from both Ni(II) and Ni(III), possibly as NiOOH surface layers on the NiO particles[94,95] or as Ni−N_x sites.[96] Shape fitting of the Cu 2p XPS also reveals two reduction states (Figure S4), Cu(II) and Cu(I)/Cu(0).[82,97] The first ($2p_{3/2}$ line at 932.4 eV) could correspond to CuO or to Cu^{II}−N_x, and the second (934.1 eV) corresponds to Cu_2O or to Cu^{I}−N_x.[98] Even if metallic copper exists (it is indistinguishable from Cu(I) by XPS), it is not expected to contribute to any catalytic activity, as it would not survive long in an oxygenated environment. The Zn 2p spectrum represents only Zn(II) species (2p line at 1022.1 eV). This ion probably corresponds to ZnO[82] rather than to a Zn−N_x cluster,[99] which is rare according to the N 1s XPS (Figure S3). The Mo 3d spectrum reveals pure Mo(VI), without any lower oxidation states (e.g., no carbides[100]). The broad peak at 232.5 eV could correspond to amorphous MoO_3[101,102] or to Mo^{VI}−N_x clusters.[103] Finally, the Pb 4f spectrum shows peaks typical to PbO, albeit shifted 0.5 eV to higher energies.[104] This shift (see Figure S4) is assigned to unreacted $Pb(NO_3)_2$,[105,106] which dissolves during catalysis.

Overall, XPS in the metal region suggests that the surface chemistry of the MO_x particles generally matches their bulk composition. Most surfaces are partially reduced, with the exception of MoO_3, V_2O_5, and ZnO where the metals are fully oxidized.

ORR Electrocatalysis. ORR electrocatalysis was used to understand how the M−N−C materials activate oxygen. We studied three aspects: activity (determined by cyclic voltammetry), selectivity for the $2e^-$ vs the $4e^-$ reduction (determined by Koutecký−Levich analysis), and stability (determined by chronoamperometry). All the M−N−C materials were active in ORR electrocatalysis, within a narrow range of overpotentials (Figure 7 and Table 2). In all cases, the pristine N-doped carbon was slightly better, with the $E_{1/2}$ within 50 mV. The MO_x particles may be blocking micropores (hindering access to surface sites) and slowing down mass transfer. Both effects may lead to lower currents and hence to lower observed onset potentials.

Table 2. Electrocatalytic ORR Activity on the M−N−C Samples[a]

M	$E^{1/2}$ (mV vs RHE)	n (e^-/O_2)	current decay[b] (%)	most probable catalytic site for O_2 reduction[c]
	834	3.26	27	N
V	813	3.15	28	$V_2O_5/V^{V/IV}$−N_x
Cr	798	3.10	19	Cr_2O_3
Mn	820	3.14	30	MnO_x
Fe	828	3.15	28	FeO_x/Fe−N_x
Co	823	2.73	45	CoO_x/Co−N_x
Ni	814	3.16	35	Ni−N_x
Cu	815	3.62	20	Cu_2O/Cu^{I}−N_x
Zn	787	3.37	23	ZnO
Mo	793	3.27	37	Mo^{VI}−N_x
Pb	780	2.74	22	N

[a]Repeated experiments deviate by <5%. [b]Current decay reported after 8 h of continuous operation. [c]See text for assignment of the most probable active sites.

To quantify the blocking, we focused on Pb−N−C. Neither PbO or Pb−N_x clusters have any ORR activity, here or in the literature. Thus, doping by Pb has a purely blocking effect on

DOI: 10.1021/acscatal.8b01045
ACS Catal. 2018, 8, 8618−8629

O_2 activating sites. The specific surface area of Pb−N−C, measured by N_2 sorption and analyzed by BET, decreases from 1570 m^2/gr in the pristine carbon to 520 m^2/gr in Pb−N−C. This drop corresponds to surface blocking by PbO particles. It should be similar in magnitude for all similarly sized MO_x particles (cf. Figure 2), with the catalytic activity of each metal offsetting this blocking.

Chronoamperometry reveals 19−45% drops in activity after 8 h of oxygen reduction (Figure 7b and Table 2). The pristine N-doped carbon decays to a stable current, due to its gradual oxygenation.[107] All M−N−C catalysts also decay over time, sometimes after an initial rise (e.g., Ni, Cr, and Cu). This decay can be related to leaching out of $M-N_x$ centers and/or the dissolution of MO_x particles. In describing MO_x dissolution, solubility constants fall short, because the particles' composition is mostly mixed. Instead, we use Pourbaix diagrams to identify thermodynamically stable phases for a given element at a range of pH values and applied potentials.[108] Here, the Pourbaix diagrams describe narrow belts at the base of the MO_x particles, because these are the regions both exposed to solution and electrically wired to the external circuit. These regions, responsible for the ORR activity, experience an applied potential of −0.36 V vs normal hydrogen electrode (NHE), and an effective pH of 13 to ∼14−15 (because alkaline ORR generates hydroxides locally).[109] The more insulated regions at the top of the particles are harder to describe by this approach, because their potential is ill-defined. Pourbaix diagrams (Figure S5) predict that all metals dissolve under these conditions, yielding oxo or hydroxy(oxo) anions, namely, $HV_2O_5^-$, CrO_2^-, $HMnO_4^{2-}$, $HFeO_2^-$, $HCoO_2^-$, $HNiO_2^-$, $HCuO_2^-$, $HZnO_2^-$, MoO_4^{2-}, and $HPbO_2^-$. This dissolution cannot be correlated to the ORR activity, because it may simultaneously (1) clear blocked sites, (2) destroy catalytic surface layers, or, conversely, (3) expose better catalytic layers.

The most active codopants in this study are based on Fe and Co. Both the oxide particles (Fe_2O_3, Fe_3O_4, CoO, and Co_3O_4) and the surface-embedded $Fe-N_x$ and $Co-N_x$ clusters can contribute to ORR electrocatalysis.[15,74,110] However, the ORR peak is sharper for Co−N−C than for Fe−N−C, suggesting a narrower distribution of active sites. The Co−N−C also decays faster in activity than Fe−N−C, possibly reflecting their difference in selectivity, as observed both here and elsewhere.[74] M−N−C catalysts can reduce O_2 by either $2e^-$ (yielding HO_2^-) or $4e^-$ (to OH^-). The number of electrons transferred per O_2 molecule (n) is 2.7 for Co−N−C and 3.2 for Fe−N−C. Thus, the products of ORR contain a higher HO_2^-/OH^- ratio for Co−N−C than for Fe−N−C. Peroxides can corrode metal-doped carbons, destroying their ORR activity.[12,111] Both $Mn-N_x$ clusters and MnO_x particles are known ORR electrocatalysts,[74,112] yet XPS shows little Mn−N binding, suggesting that MnO_x phases (Mn_3O_4, MnO_2, Mn_5O_8, or Mn_2O_3) contribute more to O_2 activation in the Mn−N−C catalyst.

The Cu−N−C catalyst is highly active, closely following the first metals. In nature, the tricopper center in the *lacasse* enzyme has excellent ORR performance. Many synthetic complexes and particles of copper show ORR activity.[113] Copper is exceptionally active toward alcohol oxidation (Figure 8), suggesting that the reaction is not limited by the O_2 activation rates. The copper in the Cu−N−C sample starts as a mixture of CuO, Cu_2O, and/or Cu(0). According to the Pourbaix diagram, CuO first dissolves to $HCuO_2^-$ and is then reduced to Cu_2O (reduction to Cu(0) is unlikely in an oxygenated solution[114,115]). Interestingly, the stepwise changes in the chronoamperogram may reflect these reductions (Figure 7b). If we think of the first 2 h of ORR as a "pretreatment" step, then the Cu(I)−N−C catalyst has the highest stability by far. The catalytic site could be either Cu_2O or Cu^I-N_x, because both are active toward the ORR.[113−115]

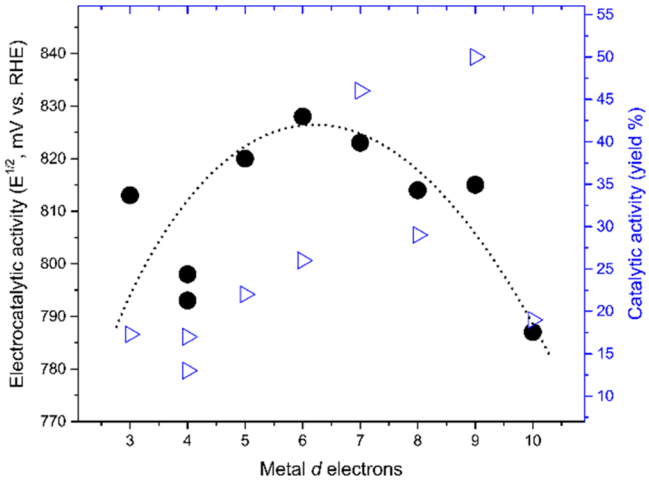

Figure 8. Comparing the catalytic activity of M−N−C samples for electrocatalytic O_2 reduction (black circles; dotted line for qualitative average) and catalytic oxidation of cinnamyl alcohol by molecular O_2 (blue triangles).[4]

The high ORR activity of the Ni−N−C and V−N−C catalysts is surprising. Neither NiO, NiOOH, or $Ni-N_4$ macrocycles are good ORR electrocatalysts.[74,116−119] NiO_x particles typically reduce O_2 only by $2e^-$, whereas we see n = 3.16 e^-/O_2. Thus, the $Ni-N_x$ sites in the Ni−N−C catalysts contribute more to the ORR than the NiO and/or NiOOH particles. Similarly, V_2O_5 particles are unlikely to be good ORR catalysts,[120] suggesting that it is the V(IV) surface layer, detected by XPS and TPR, that drives the catalysis.[121] Little is known about $V-N_x$ centers for alkaline ORR catalysis; such activity was only observed for homogeneous vanadium complexes in acidic media.[121]

Cr−N−C has mediocre ORR activity, like other Cr_2O_3/carbon composites and $Cr-N_4$ macrocycles.[122,123] Typically, CrO_x particles prefer the $4e^-$ reduction, while $Cr-N_x$ clusters are selective toward the $2e^-$ reduction. Our Cr−N−C catalyst shows n = 3.1, suggesting that the Cr_2O_3 particles are more significant for ORR electrocatalysis. Moreover, the rise in ORR activity after ∼5 h (Figure 7b) suggests that initial dissolution of the CrO_3 surface layer (detected by TPR) improves activity.

The ORR activity of the Mo−N−C catalyst approaches that of Cr−N−C. Because MoO_3 is inactive in ORR,[76] the activity is assigned to the prominent $Mo-N_x$ sites.[124] In the Zn−N−C material, conversely, Zn−N binding is weak, suggesting that ZnO contributes to the meager ORR activity observed.[119,125,126]

In future studies, we hope to refine the active site assignment by using selective leaching or selective reduction of MO_x particles, or the selective blocking of $M-N_x$ sites, in order to decouple the interactions in their activities. This should lead to better control materials, which are otherwise hard to produce.

O_2 Activation—From ORR to Alcohol Oxidation. The ORR activity follows a "volcano"-type trend with respect to the number of d-electrons (Figure 8). The volcano peak is on Fe−N−C. This behavior matches most systematic comparisons of

DOI: 10.1021/acscatal.8b01045
ACS Catal. 2018, 8, 8618−8629

third-row transition metals as electrocatalysts for alkaline ORR.[74] This alignment with the literature further supports the hypothesis that the drop in ORR activity (relative to the pristine N-doped carbon) that was observed for all metal dopants is indeed a systematic effect—despite the small differences in electrocatalytic activity ($E^{1/2}$ spreads over 50 mV). Interestingly, vanadium outperforms the trend, calling for additional studies of this novel V−N−C catalyst.

Similarly, the catalytic activity of the M−N−C materials toward cinnamyl alcohol oxidation is volcano-shaped.[4] The peak is centered on Co or Cu, with one outlier (Cu or Co, respectively). This similarity between the volcanoes suggests that O_2 activation is the reaction bottleneck. The outlier must have excellent ORR on its own to overcome this bottleneck; both Co and Cu fit this description, although Co is more active. Previous studies suggest that ORR activity is correlated to O_2 activation in catalytic transformations.[30−33] The qualitative match between the two volcano plots lends some support to this hypothesis. However, the center of the peak is shifted by either 1 (Co) or 3 (Cu) d-electrons, when comparing the catalytic and electrocatalytic systems.

The active site assignments (Table 2) can direct catalyst design. In catalysts where O_2 activation is done primarily on the oxide particles (e.g., Cr_2O_3, ZnO, and MnO_x), the oxide surface area should be maximized. This calls for an optimization of the impregnation procedure, to minimize particle size and maximize particle loading up to when they start blocking mass transport. Moreover, the carbon is merely an idle support here, enabling particle dispersion and material handling. Carbon optimization efforts should then focus on pore design (for easing flow) and promoting graphitization (to boost conductivity and stability).

Conversely, if O_2 is activated at the surface-embedded M−N_x clusters, then the M−N−C material is a tandem catalyst. During catalytic alcohol oxidation, sites such as $V^{V/IV}$−, Fe−, Co−, Ni−, Cu^{I}−, and Mo^{VI}−N_x activate O_2, while the MO_x particles bind and oxidize the alcohol. We have recently analyzed this situation in depth, focusing on the interaction between the two types of active sites.[127] This interaction can be chemical (exchange of intermediates) or electronic (charge transfer). Its efficiency determines the dimensions of the so-called "active doughnut", the toroidal volume at the base of the particles, where the reaction occurs during the exchange step. In these tandem catalysts, the loading of oxide particles cannot be maximized or they will block M−N_x sites. Rather, the particle dispersion needs to be carefully tuned, aiming at (1) maximum exposure of both types of sites and (2) interparticle distances optimized to the lifetimes and diffusivities of reaction intermediates. Furthermore, carbon graphitization (and hence conductivity) is more important in tandem catalysts, as it determines the rate of charge transfer between redox sites.

CONCLUSIONS

We studied the structure and catalytic activity of 10 carbon materials, codoped by nitrogen and transition metals. These materials are promising catalysts for heterogeneous oxidations with molecular oxygen. To identify the active sites for O_2 activation, we separated the two doping processes by loading the metals onto an existing N-doped carbon (using incipient wetness impregnation). All resulting M−N−C catalyts were composed of a porous carbon doped by nitrogen, metal−nitrogen coordination clusters, and metal oxide particles. The extent of the metal−nitrogen binding was assessed by XPS and found to be strongest for Cr-, Fe-, Co-, Ni-, Cu-, and Mo-based carbons. The metal oxide particles were found to be partially reduced, to be mostly amorphous (excluding Mn_3O_4, CuO, and ZnO phases), and to range in size between 100−400 nm.

To understand how these materials activate oxygen, we studied their activity, selectivity, and stability in electrocatalytic alkaline ORR. The activity order was Fe > Co > Mn > Cu ≈ Ni ≈ V > Cr > Mo > Zn > Pb. The M−N−C catalysts displayed medium selectivity toward the $4e^-/O_2$ reduction, as compared to the $2e^-/O_2$ reduction. All catalysts degraded during ORR, partially explained by the solubility of oxides in base. By correlating the ORR activity to material data and literature knowledge, we assigned probable active sites for O_2 activation. In some, these are M−N_x centers (Mo and Ni), in some they are MO_x particles (Cr, Mn, and Zn), and there are probably a combination of both in the most active materials (V, Fe, Co, and Cu). The oxide particles block some of the surface sites. On the basis of these assignments, we proposed design guidelines for improving the performance of these M−N−C catalysts in the ORR.

ASSOCIATED CONTENT

Supporting Information

The Supporting Information is available free of charge on the ACS Publications website at DOI: 10.1021/acscatal.8b01045.

Scanning electron micrographs, X-ray diffractograms, and XPS spectra of the M−N−C composites, mathematically deconvoluted X-ray photoelectron spectra of Cu 2p and Pb 4f, and Pourbaix diagrams of the studied metals (PDF)

AUTHOR INFORMATION

Corresponding Author

*E-mail: eisenberg@technion.ac.il.

ORCID

David Eisenberg: 0000-0001-5568-337X

Notes

The authors declare no competing financial interest.

ACKNOWLEDGMENTS

We thank Mr. Pierre Mettraux (EPFL, Switzerland) for XPS measurements, Mr. Eliyahu Farber (Technion, Israel) for SEM measurements, and Mr. Norbert J. Geels (University of Amsterdam, The Netherlands) for N_2 porosimetry measurements.

REFERENCES

(1) Zhang, P.; Gong, Y.; Li, H.; Chen, Z.; Wang, Y. Solvent-Free Aerobic Oxidation of Hydrocarbons and Alcohols with Pd@N-Doped Carbon from Glucose. *Nat. Commun.* **2013**, *4*, 1593.

(2) Jagadeesh, R. V.; Junge, H.; Pohl, M.-M.; Radnik, J.; Brückner, A.; Beller, M. Selective Oxidation of Alcohols to Esters Using Heterogeneous Co_3O_4−N@C Catalysts under Mild Conditions. *J. Am. Chem. Soc.* **2013**, *135*, 10776−10782.

(3) He, L.; Weniger, F.; Neumann, H.; Beller, M. Synthesis, Characterization, and Application of Metal Nanoparticles Supported on Nitrogen-Doped Carbon: Catalysis beyond Electrochemistry. *Angew. Chem., Int. Ed.* **2016**, *55*, 12582−12594.

(4) Slot, T. K.; Eisenberg, D.; van Noordenne, D.; Jungbacker, P.; Rothenberg, G. Cooperative Catalysis for Selective Alcohol Oxidation with Molecular Oxygen. *Chem. - Eur. J.* **2016**, *22*, 12307−12311.

(5) Xie, J.; Yin, K.; Serov, A.; Artyushkova, K.; Pham, H. N.; Sang, X.; Unocic, R. R.; Atanassov, P.; Datye, A. K.; Davis, R. J. Selective

DOI: 10.1021/acscatal.8b01045
ACS Catal. 2018, 8, 8618−8629

Aerobic Oxidation of Alcohols over Atomically-Dispersed Non-Precious Metal Catalysts. *ChemSusChem* **2017**, *10*, 359−362.
(6) Denekamp, I. M.; Antens, M.; Slot, T. K.; Rothenberg, G. Selective Catalytic Oxidation of Cyclohexene with Molecular Oxygen: Radical Versus Nonradical Pathways. *ChemCatChem* **2018**, *10*, 1035−1041.
(7) Liu, Y.; Zhang, N.; Jiao, L.; Chen, J. Tin Nanodots Encapsulated in Porous Nitrogen-Doped Carbon Nanofibers as a Free-Standing Anode for Advanced Sodium-Ion Batteries. *Adv. Mater.* **2015**, *27*, 6702−6707.
(8) Balogun, M.-S.; Luo, Y.; Qiu, W.; Liu, P.; Tong, Y. A Review of Carbon Materials and Their Composites with Alloy Metals for Sodium Ion Battery Anodes. *Carbon* **2016**, *98*, 162−178.
(9) Yan, J.; Wang, Q.; Wei, T.; Fan, Z. Recent Advances in Design and Fabrication of Electrochemical Supercapacitors with High Energy Densities. *Adv. Energy Mater.* **2014**, *4*, 1300816.
(10) Cao, F.; Zhao, M.; Yu, Y.; Chen, B.; Huang, Y.; Yang, J.; Cao, X.; Lu, Q.; Zhang, X.; Zhang, Z.; et al. Synthesis of Two-Dimensional $CoS_{1.097}$/Nitrogen-Doped Carbon Nanocomposites Using Metal−Organic Framework Nanosheets as Precursors for Supercapacitor Application. *J. Am. Chem. Soc.* **2016**, *138*, 6924−6927.
(11) Wu, G.; More, K. L.; Johnston, C. M.; Zelenay, P. High-Performance Electrocatalysts for Oxygen Reduction Derived from Polyaniline, Iron, and Cobalt. *Science* **2011**, *332*, 443−447.
(12) Trogadas, P.; Fuller, T. F.; Strasser, P. Carbon as Catalyst and Support for Electrochemical Energy Conversion. *Carbon* **2014**, *75*, 5−42.
(13) Shao, M.; Chang, Q.; Dodelet, J.-P.; Chenitz, R. Recent Advances in Electrocatalysts for Oxygen Reduction Reaction. *Chem. Rev.* **2016**, *116*, 3594−3657.
(14) Sarapuu, A.; Kibena-Põldsepp, E.; Borghei, M.; Tammeveski, K. Electrocatalysis of Oxygen Reduction on Heteroatom-Doped Nanocarbons and Transition Metal−nitrogen−carbon Catalysts for Alkaline Membrane Fuel Cells. *J. Mater. Chem. A* **2018**, *6*, 776−804.
(15) Chisaka, M. Transition Metal Oxide, Oxynitride, and Nitride Electrocatalysts with and without Supports for Polymer Electrolyte Fuel Cell Cathodes. *Electrocatalysts Low Temp. Fuel Cells Fundam. Recent Trends* **2017**, 423.
(16) Marsh, H.; Menendez, R. Chapter 2: Mechanisms of Formation of Isotropic and Anisotropic Carbons. In *Introduction to Carbon Science*; Butterworth-Heinemann: 1989; pp 37−73.
(17) Sen, R.; Govindaraj, A.; Rao, C. N. R. Carbon Nanotubes by the Metallocene Route. *Chem. Phys. Lett.* **1997**, *267*, 276−280.
(18) Shen, K.; Chen, X.; Chen, J.; Li, Y. Development of MOF-Derived Carbon-Based Nanomaterials for Efficient Catalysis. *ACS Catal.* **2016**, *6*, 5887−5903.
(19) Wu, H. B.; Xia, B. Y.; Yu, L.; Yu, X.-Y.; Lou, X. W. Porous Molybdenum Carbide Nano-Octahedrons Synthesized via Confined Carburization in Metal-Organic Frameworks for Efficient Hydrogen Production. *Nat. Commun.* **2015**, *6*, 6512.
(20) Sevilla, M.; Fuertes, A. B. A General and Facile Synthesis Strategy towards Highly Porous Carbons: Carbonization of Organic Salts. *J. Mater. Chem. A* **2013**, *1*, 13738−13741.
(21) Morishita, T.; Tsumura, T.; Toyoda, M.; Przepiórski, J.; Morawski, A. W.; Konno, H.; Inagaki, M. A Review of the Control of Pore Structure in MgO-Templated Nanoporous Carbons. *Carbon* **2010**, *48*, 2690−2707.
(22) Wiggins-Camacho, J. D.; Stevenson, K. J. Effect of Nitrogen Concentration on Capacitance, Density of States, Electronic Conductivity, and Morphology of N-Doped Carbon Nanotube Electrodes. *J. Phys. Chem. C* **2009**, *113*, 19082−19090.
(23) Yang, W.; Fellinger, T.-P.; Antonietti, M. Efficient Metal-Free Oxygen Reduction in Alkaline Medium on High-Surface-Area Mesoporous Nitrogen-Doped Carbons Made from Ionic Liquids and Nucleobases. *J. Am. Chem. Soc.* **2011**, *133*, 206−209.
(24) Biemolt, J.; Denekamp, I. M.; Slot, T. K.; Rothenberg, G.; Eisenberg, D. Boosting the Supercapacitance of Nitrogen-Doped Carbon by Tuning Surface Functionalities. *ChemSusChem* **2017**, *10*, 4018−4024.
(25) Guo, D.; Shibuya, R.; Akiba, C.; Saji, S.; Kondo, T.; Nakamura, J. Active Sites of Nitrogen-Doped Carbon Materials for Oxygen Reduction Reaction Clarified Using Model Catalysts. *Science* **2016**, *351*, 361−365.
(26) Chung, H. T.; Cullen, D. A.; Higgins, D.; Sneed, B. T.; Holby, E. F.; More, K. L.; Zelenay, P. Direct Atomic-Level Insight into the Active Sites of a High-Performance PGM-Free ORR Catalyst. *Science* **2017**, *357*, 479−484.
(27) Ding, Z.; Chen, X.; Antonietti, M.; Wang, X. Synthesis of Transition Metal-Modified Carbon Nitride Polymers for Selective Hydrocarbon Oxidation. *ChemSusChem* **2011**, *4*, 274−281.
(28) Deng, J.; Song, H.-J.; Cui, M.-S.; Du, Y.-P.; Fu, Y. Aerobic Oxidation of Hydroxymethylfurfural and Furfural by Using Heterogeneous Co_xO_y−N@C Catalysts. *ChemSusChem* **2014**, *7*, 3334−3340.
(29) Jagadeesh, R. V.; Junge, H.; Beller, M. Green Synthesis of Nitriles Using Non-Noble Metal Oxides-Based Nanocatalysts. *Nat. Commun.* **2014**, *5*, 4123.
(30) Zope, B. N.; Hibbitts, D. D.; Neurock, M.; Davis, R. J. Reactivity of the Gold/Water Interface During Selective Oxidation Catalysis. *Science* **2010**, *330*, 74−78.
(31) Zhou, C.; Chen, Y.; Guo, Z.; Wang, X.; Yang, Y. Promoted Aerobic Oxidation of Benzyl Alcohol on CNT Supported Platinum by Iron Oxide. *Chem. Commun.* **2011**, *47*, 7473−7475.
(32) Tan, H. T.; Chen, Y.; Zhou, C.; Jia, X.; Zhu, J.; Chen, J.; Rui, X.; Yan, Q.; Yang, Y. Palladium Nanoparticles Supported on Manganese Oxide−CNT Composites for Solvent-Free Aerobic Oxidation of Alcohols: Tuning the Properties of Pd Active Sites Using MnO_x. *Appl. Catal., B* **2012**, *119*−*120*, 166−174.
(33) Donoeva, B.; Masoud, N.; de Jongh, P. E. Carbon Support Surface Effects in the Gold-Catalyzed Oxidation of 5-Hydroxymethylfurfural. *ACS Catal.* **2017**, *7*, 4581−4591.
(34) Eisenberg, D.; Stroek, W.; Geels, N. J.; Sandu, C. S.; Heller, A.; Yan, N.; Rothenberg, G. A Simple Synthesis of an N-Doped Carbon ORR Catalyst: Hierarchical Micro/Meso/Macro Porosity and Graphitic Shells. *Chem. - Eur. J.* **2016**, *22*, 501−505.
(35) Eisenberg, D.; Stroek, W.; Geels, N. J.; Tanase, S.; Ferbinteanu, M.; Teat, S. J.; Mettraux, P.; Yan, N.; Rothenberg, G. A Rational Synthesis of Hierarchically Porous, N-Doped Carbon from Mg-Based MOFs: Understanding the Link between Nitrogen Content and Oxygen Reduction Electrocatalysis. *Phys. Chem. Chem. Phys.* **2016**, *18*, 20778−20783.
(36) Eisenberg, D.; Prinsen, P.; Geels, N. J.; Stroek, W.; Yan, N.; Hua, B.; Luo, J.-L.; Rothenberg, G. The Evolution of Hierarchical Porosity in Self-Templated Nitrogen-Doped Carbons and Its Effect on Oxygen Reduction Electrocatalysis. *RSC Adv.* **2016**, *6*, 80398−80407.
(37) Hutchings, G. J.; Védrine, J. C. Heterogeneous Catalyst Preparation. In *Basic Principles in Applied Catalysis*; Springer Series in Chemical Physics; Springer: Berlin/Heidelberg, 2004; pp 215−258.
(38) Arnoldy, P.; De Jonge, J. C. M.; Moulijn, J. A. Temperature-Programed Reduction of Molybdenum(VI) Oxide and Molybdenum-(IV) Oxide. *J. Phys. Chem.* **1985**, *89*, 4517−4526.
(39) Zhang, H.; Lancelot, C.; Chu, W.; Hong, J.; Khodakov, A. Y.; Chernavskii, P. A.; Zheng, J.; Tong, D. The Nature of Cobalt Species in Carbon Nanotubes and Their Catalytic Performance in Fischer−Tropsch Reaction. *J. Mater. Chem.* **2009**, *19*, 9241−9249.
(40) Ren, J.; Wang, W.; Qin, Z.; Pei, Y.; Wang, D.; Lin, J.; Li, Z. Oxidative Carbonylation of Methanol to Dimethyl Carbonate over Cu/AC Catalysts Prepared by Microwave Irradiation: Effect of La and Zr Promoters. *Indian J. Chem. Technol.* **2016**, *23*, 384−391.
(41) Airaksinen, S. M. K.; Krause, A. O. I.; Sainio, J.; Lahtinen, J.; Chao, K.; Guerrero-Pérez, M. O.; Bañares, M. A. Reduction of Chromia/Alumina Catalyst Monitored by DRIFTS-Mass Spectrometry and TPR-Raman Spectroscopy. *Phys. Chem. Chem. Phys.* **2003**, *5*, 4371−4377.
(42) Xia, Y.; Dai, H.; Jiang, H.; Deng, J.; He, H.; Au, C. T. Mesoporous Chromia with Ordered Three-Dimensional Structures for the Complete Oxidation of Toluene and Ethyl Acetate. *Environ. Sci. Technol.* **2009**, *43*, 8355−8360.

DOI: 10.1021/acscatal.8b01045
ACS Catal. 2018, 8, 8618−8629

(43) Węgrzyniak, A.; Jarczewski, S.; Wach, A.; Hędrzak, E.; Kuśtrowski, P.; Michorczyk, P. Catalytic Behaviour of Chromium Oxide Supported on CMK-3 Carbon Replica in the Dehydrogenation Propane to Propene. *Appl. Catal., A* **2015**, *508*, 1−9.
(44) Kapteijn, F.; Singoredjo, L.; Andreini, A.; Moulijn, J. A. Activity and Selectivity of Pure Manganese Oxides in the Selective Catalytic Reduction of Nitric Oxide with Ammonia. *Appl. Catal., B* **1994**, *3*, 173−189.
(45) Hughes, I. S. C.; Newman, J. O. H.; Bond, G. C. The Characterisation of Unsupported Iron and Manganese-Promoted Iron Catalysts by X-Ray Photoelectron Spectroscopy and Temperature-Programmed Reduction. *Appl. Catal.* **1987**, *30*, 303−311.
(46) Wang, L.; Huang, B.; Su, Y.; Zhou, G.; Wang, K.; Luo, H.; Ye, D. Manganese Oxides Supported on Multi-Walled Carbon Nanotubes for Selective Catalytic Reduction of NO with NH_3: Catalytic Activity and Characterization. *Chem. Eng. J.* **2012**, *192*, 232−241.
(47) Tang, Q.; Huang, X.; Chen, Y.; Liu, T.; Yang, Y. Characterization and Catalytic Application of Highly Dispersed Manganese Oxides Supported on Activated Carbon. *J. Mol. Catal. A: Chem.* **2009**, *301*, 24−30.
(48) Brown, R.; Cooper, M. E.; Whan, D. A. Temperature Programmed Reduction of Alumina-Supported Iron, Cobalt and Nickel Bimetallic Catalysts. *Appl. Catal.* **1982**, *3*, 177−186.
(49) Tiernan, M. J.; Barnes, P. A.; Parkes, G. M. B. Reduction of Iron Oxide Catalysts: The Investigation of Kinetic Parameters Using Rate Perturbation and Linear Heating Thermoanalytical Techniques. *J. Phys. Chem. B* **2001**, *105*, 220−228.
(50) Ma, W.; Kugler, E. L.; Wright, J.; Dadyburjor, D. B. Mo−Fe Catalysts Supported on Activated Carbon for Synthesis of Liquid Fuels by the Fischer−Tropsch Process: Effect of Mo Addition on Reducibility, Activity, and Hydrocarbon Selectivity. *Energy Fuels* **2006**, *20*, 2299−2307.
(51) Abbaslou, R. M. M.; Tavassoli, A.; Soltan, J.; Dalai, A. K. Iron Catalysts Supported on Carbon Nanotubes for Fischer−Tropsch Synthesis: Effect of Catalytic Site Position. *Appl. Catal., A* **2009**, *367*, 47−52.
(52) Lu, J.; Yang, L.; Xu, B.; Wu, Q.; Zhang, D.; Yuan, S.; Zhai, Y.; Wang, X.; Fan, Y.; Hu, Z. Promotion Effects of Nitrogen Doping into Carbon Nanotubes on Supported Iron Fischer−Tropsch Catalysts for Lower Olefins. *ACS Catal.* **2014**, *4*, 613−621.
(53) Fu, T.; Lv, J.; Li, Z. Effect of Carbon Porosity and Cobalt Particle Size on the Catalytic Performance of Carbon Supported Cobalt Fischer−Tropsch Catalysts. *Ind. Eng. Chem. Res.* **2014**, *53*, 1342−1350.
(54) Ni, W.; Liu, S.; Fei, Y.; He, Y.; Ma, X.; Lu, L.; Deng, Y. CoO@Co and N-Doped Mesoporous Carbon Composites Derived from Ionic Liquids as Cathode Catalysts for Rechargeable Lithium−Oxygen Batteries. *J. Mater. Chem. A* **2016**, *4*, 7746−7753.
(55) Mile, B.; Stirling, D.; Zammitt, M. A.; Lovell, A.; Webb, M. The Location of Nickel Oxide and Nickel in Silica-Supported Catalysts: Two Forms of "NiO" and the Assignment of Temperature-Programmed Reduction Profiles. *J. Catal.* **1988**, *114*, 217−229.
(56) Moreno-Tost, R.; Santamaría-González, J.; Maireles-Torres, P.; Rodríguez-Castellón, E.; Jiménez-López, A. Nickel Oxide Supported on Zirconium-Doped Mesoporous Silica for Selective Catalytic Reduction of NO with NH_3. *J. Mater. Chem.* **2002**, *12*, 3331−3336.
(57) Ren, Y.; Bruce, P. G.; Ma, Z. Solid-Solid Conversion of Ordered Crystalline Mesoporous Metal Oxides under Reducing Atmosphere. *J. Mater. Chem.* **2011**, *21*, 9312−9318.
(58) Calafat, A.; Laine, J.; López-Agudo, A.; Palacios, J. M. Effect of Surface Oxidation of the Support on the Thiophene Hydrodesulfurization Activity of Mo, Ni, and NiMo Catalysts Supported on Activated Carbon. *J. Catal.* **1996**, *162*, 20−30.
(59) Lensveld, D. J.; Gerbrand Mesu, J.; Jos van Dillen, A.; de Jong, K. P. Synthesis and Characterisation of MCM-41 Supported Nickel Oxide Catalysts. *Microporous Mesoporous Mater.* **2001**, *44*−*45*, 401−407.
(60) Kim, J. Y.; Rodriguez, J. A.; Hanson, J. C.; Frenkel, A. I.; Lee, P. L. Reduction of CuO and Cu_2O with H_2: H Embedding and Kinetic Effects in the Formation of Suboxides. *J. Am. Chem. Soc.* **2003**, *125*, 10684−10692.
(61) Weiqing, Z.; Xinqiang, Z.; Yanji, W.; Jiyan, Z. Synthesis of Diphenyl Carbonate by Transesterification over Lead and Zinc Double Oxide Catalyst. *Appl. Catal., A* **2004**, *260*, 19−24.
(62) Maciel, A. V.; Job, A. E.; da Nova Mussel, W.; de Brito, W.; Duarte Pasa, V. M. Bio-Hydrogen Production Based on Catalytic Reforming of Volatiles Generated by Cellulose Pyrolysis: An Integrated Process for ZnO Reduction and Zinc Nanostructures Fabrication. *Biomass Bioenergy* **2011**, *35*, 1121−1129.
(63) Feng, L.; Li, X.; Dadyburjor, D. B.; Kugler, E. L. A Temperature-Programmed-Reduction Study on Alkali-Promoted, Carbon-Supported Molybdenum Catalysts. *J. Catal.* **2000**, *190*, 1−13.
(64) Mordenti, D.; Brodzki, D.; Djéga-Mariadassou, G. New Synthesis of Mo_2C 14 Nm in Average Size Supported on a High Specific Surface Area Carbon Material. *J. Solid State Chem.* **1998**, *141*, 114−120.
(65) Wendt, G.; Meinecke, C.-D.; Schmitz, W. Oxidative Dimerization of Methane on Lead Oxide−Alumina Catalysts. *Appl. Catal.* **1988**, *45*, 209−220.
(66) Koranne, M. M.; Goodwin, J. G.; Marcelin, G. Characterization of Silica- and Alumina-Supported Vanadia Catalysts Using Temperature Programmed Reduction. *J. Catal.* **1994**, *148*, 369−377.
(67) Besselmann, S.; Freitag, C.; Hinrichsen, O.; Muhler, M. Temperature-Programmed Reduction and Oxidation Experiments with V_2O_5/TiO_2 Catalysts. *Phys. Chem. Chem. Phys.* **2001**, *3*, 4633−4638.
(68) Ji, D.; Liu, S.; Wang, Q.; Xu, L. Novel Catalysis of TiO_2 for the Catalytic Alcohols Synthesis from CO and H_2O. *Fuel Process. Technol.* **2004**, *85*, 1165−1173.
(69) Wang, S.; Li, C.; Xiao, Z.; Chen, T.; Wang, G. Highly Efficient and Stable PbO-ZrO_2 Catalyst for the Disproportionation of Methyl Phenyl Carbonate to Synthesize Diphenyl Carbonate. *J. Mol. Catal. A: Chem.* **2016**, *420*, 26−33.
(70) Cedeño Caero, L.; F, J.; A, N.; Gutiérrez-Alejandre, A. Oxidative Desulfurization of Synthetic Diesel Using Supported Catalysts. *Catal. Today* **2006**, *116*, 562−568.
(71) Fattahi, M.; Kazemeini, M.; Khorasheh, F.; Rashidi, A. M. Vanadium Pentoxide Catalyst over Carbon-Based Nanomaterials for the Oxidative Dehydrogenation of Propane. *Ind. Eng. Chem. Res.* **2013**, *52*, 16128−16141.
(72) Rivoira, L.; Juárez, J.; Falcón, H.; Gómez Costa, M.; Anunziata, O.; Beltramone, A. Vanadium and Titanium Oxide Supported on Mesoporous CMK-3 as New Catalysts for Oxidative Desulfurization. *Catal. Today* **2017**, *282*, 123−132.
(73) Eisenberg, D.; Prinsen, P.; Geels, N. J.; Stroek, W.; Yan, N.; Hua, B.; Luo, J.-L.; Rothenberg, G. The Evolution of Hierarchical Porosity in Self-Templated Nitrogen-Doped Carbons and Its Effect on Oxygen Reduction Electrocatalysis. *RSC Adv.* **2016**, *6*, 80398−80407.
(74) *Electrochemistry of N_4 Macrocyclic Metal Complexes*; Zagal, J. H., Bedioui, F., Eds.; Springer International Publishing: Cham, 2016.
(75) Gokhale, R.; Thapa, S.; Artyushkova, K.; Giri, R.; Atanassov, P. Fully Synthetic Approach towards Transition Metal-Nitrogen-Carbon Oxygen Reduction Electrocatalysts. *ACS Appl. Energy Mater.* **2018**. DOI: 10.1021/acsaem.8b00537
(76) Yavuz, E.; Özdokur, K. V.; Çakar, İ.; Koçak, S.; Ertaş, F. N. Electrochemical Preparation, Characterization of Molybdenum-Oxide/Platinum Binary Catalysts and Its Application to Oxygen Reduction Reaction in Weakly Acidic Medium. *Electrochim. Acta* **2015**, *151*, 72−80.
(77) Jaouen, F.; Herranz, J.; Lefèvre, M.; Dodelet, J.-P.; Kramm, U. I.; Herrmann, I.; Bogdanoff, P.; Maruyama, J.; Nagaoka, T.; Garsuch, A.; et al. Cross-Laboratory Experimental Study of Non-Noble-Metal Electrocatalysts for the Oxygen Reduction Reaction. *ACS Appl. Mater. Interfaces* **2009**, *1*, 1623−1639.
(78) Kramm, U. I.; Abs-Wurmbach, I.; Herrmann-Geppert, I.; Radnik, J.; Fiechter, S.; Bogdanoff, P. Influence of the Electron-Density of FeN_4-Centers Towards the Catalytic Activity of Pyrolyzed

DOI: 10.1021/acscatal.8b01045
ACS Catal. 2018, 8, 8618−8629

FeTMPPCl-Based ORR-Electrocatalysts. *J. Electrochem. Soc.* **2011**, *158*, B69−B78.
(79) Karweik, D. H.; Winograd, N. Nitrogen Charge Distributions in Free-Base Porphyrins, Metalloporphyrins, and Their Reduced Analogs Observed by X-Ray Photoelectron Spectroscopy. *Inorg. Chem.* **1976**, *15*, 2336−2342.
(80) Goellner, V.; Armel, V.; Zitolo, A.; Fonda, E.; Jaouen, F. Degradation by Hydrogen Peroxide of Metal-Nitrogen-Carbon Catalysts for Oxygen Reduction. *J. Electrochem. Soc.* **2015**, *162*, H403−H414.
(81) Demeter, M.; Neumann, M.; Reichelt, W. Mixed-Valence Vanadium Oxides Studied by XPS. *Surf. Sci.* **2000**, *454-456*, 41−44.
(82) Biesinger, M. C.; Lau, L. W. M.; Gerson, A. R.; Smart, R. S. C. Resolving Surface Chemical States in XPS Analysis of First Row Transition Metals, Oxides and Hydroxides: Sc, Ti, V, Cu and Zn. *Appl. Surf. Sci.* **2010**, *257*, 887−898.
(83) Aronniemi, M.; Sainio, J.; Lahtinen, J. Chemical State Quantification of Iron and Chromium Oxides Using XPS: The Effect of the Background Subtraction Method. *Surf. Sci.* **2005**, *578*, 108−123.
(84) Girovsky, J.; Tarafder, K.; Wäckerlin, C.; Nowakowski, J.; Siewert, D.; Hählen, T.; Wäckerlin, A.; Kleibert, A.; Ballav, N.; Jung, T. A.; et al. Antiferromagnetic Coupling of Cr-Porphyrin to a Bare Co Substrate. *Phys. Rev. B: Condens. Matter Mater. Phys.* **2014**, *90*, 220404.
(85) Yadav, K. K.; Kumar, A.; Sahu, D. K.; Lohiya, R.; Srivastava, S. Synthesis and Characterisation of Chromium (III) Compounds with Tetradentate N_4 Macrocyclic Ligands. *Int. J. Res. Chem. Environ.* **2018**, *8*, 37−43.
(86) Pröll, J.; Kohler, R.; Torge, M.; Ulrich, S.; Ziebert, C.; Bruns, M.; Seifert, H. J.; Pfleging, W. Laser Microstructuring and Annealing Processes for Lithium Manganese Oxide Cathodes. *Appl. Surf. Sci.* **2011**, *257*, 9968−9976.
(87) Lee, J. H.; Sa, Y. J.; Kim, T. K.; Moon, H. R.; Joo, S. H. A Transformative Route to Nanoporous Manganese Oxides of Controlled Oxidation States with Identical Textural Properties. *J. Mater. Chem. A* **2014**, *2*, 10435−10443.
(88) Grissa, R.; Martinez, H.; Cotte, S.; Galipaud, J.; Pecquenard, B.; Cras, F. L. Thorough XPS Analyses on Overlithiated Manganese Spinel Cycled around the 3V Plateau. *Appl. Surf. Sci.* **2017**, *411*, 449−456.
(89) Cao, R.; Thapa, R.; Kim, H.; Xu, X.; Gyu Kim, M.; Li, Q.; Park, N.; Liu, M.; Cho, J. Promotion of Oxygen Reduction by a Bio-Inspired Tethered Iron Phthalocyanine Carbon Nanotube-Based Catalyst. *Nat. Commun.* **2013**, *4*, 2076.
(90) Indra, A.; Menezes, P. W.; Das, C.; Göbel, C.; Tallarida, M.; Schmeißer, D.; Driess, M. A Facile Corrosion Approach to the Synthesis of Highly Active CoO_x Water Oxidation Catalysts. *J. Mater. Chem. A* **2017**, *5*, 5171−5177.
(91) Guo, L.; Gu, X.; Kang, K.; Wu, Y.; Cheng, J.; Liu, P.; Wang, T.; Su, H. Porous Nitrogen-Doped Carbon-Immobilized Bimetallic Nanoparticles as Highly Efficient Catalysts for Hydrogen Generation from Hydrolysis of Ammonia Borane. *J. Mater. Chem. A* **2015**, *3*, 22807−22815.
(92) Díaz-Fernández, D.; Méndez, J.; Bomatí-Miguel, O.; Yubero, F.; Mossanek, R. J. O.; Abbate, M.; Domínguez-Cañizares, G.; Gutiérrez, A.; Tougaard, S.; Soriano, L. The Growth of Cobalt Oxides on HOPG and SiO_2 Surfaces: A Comparative Study. *Surf. Sci.* **2014**, *624*, 145−153.
(93) Zhang, W.; Shaikh, A. U.; Tsui, E. Y.; Swager, T. M. Cobalt Porphyrin Functionalized Carbon Nanotubes for Oxygen Reduction. *Chem. Mater.* **2009**, *21*, 3234−3241.
(94) Biesinger, M. C.; Payne, B. P.; Lau, L. W. M.; Gerson, A.; Smart, R. S. C. X-Ray Photoelectron Spectroscopic Chemical State Quantification of Mixed Nickel Metal, Oxide and Hydroxide Systems. *Surf. Interface Anal.* **2009**, *41*, 324−332.
(95) Grosvenor, A. P.; Biesinger, M. C.; Smart, R. S. C.; McIntyre, N. S. New Interpretations of XPS Spectra of Nickel Metal and Oxides. *Surf. Sci.* **2006**, *600*, 1771−1779.
(96) Berríos, C.; Cárdenas-Jirón, G. I.; Marco, J. F.; Gutiérrez, C.; Ureta-Zañartu, M. S. Theoretical and Spectroscopic Study of Nickel(II) Porphyrin Derivatives. *J. Phys. Chem. A* **2007**, *111*, 2706−2714.
(97) Fu, R.; Yoshizawa, N.; Dresselhaus, M. S.; Dresselhaus, G.; Satcher, J. H.; Baumann, T. F. XPS Study of Copper-Doped Carbon Aerogels. *Langmuir* **2002**, *18*, 10100−10104.
(98) Niwa, Y. X-ray Photoelectron Spectroscopy of Reduced Porphins. *J. Chem. Phys.* **1975**, *62*, 737−738.
(99) Arellano, L. M.; Barrejón, M.; Gobeze, H. B.; Gómez-Escalonilla, M. J.; Fierro, J. L. G.; D'Souza, F.; Langa, F. Charge Stabilizing Tris(triphenylamine)-Zinc Porphyrin−carbon Nanotube Hybrids: Synthesis, Characterization and Excited State Charge Transfer Studies. *Nanoscale* **2017**, *9*, 7551−7558.
(100) Delporte, P.; Meunier, F.; Pham-Huu, C.; Vennegues, P.; Ledoux, M. J.; Guille, J. Physical Characterization of Molybdenum Oxycarbide Catalyst; TEM, XRD and XPS. *Catal. Today* **1995**, *23*, 251−267.
(101) Spevack, P. A.; McIntyre, N. S. A Raman and XPS Investigation of Supported Molybdenum Oxide Thin Films. 1. Calcination and Reduction Studies. *J. Phys. Chem.* **1993**, *97*, 11020−11030.
(102) Choi, J.-G.; Thompson, L. T. XPS Study of as-Prepared and Reduced Molybdenum Oxides. *Appl. Surf. Sci.* **1996**, *93*, 143−149.
(103) Song, S.-N.; Li, D.-M.; Wu, J.-F.; Zhuang, C.-F.; Ding, H.; Song, W.-B.; Cui, L.-F.; Cao, G.-Z.; Liu, G.-F. Syntheses and Characterization of Molybdenum/Zinc Porphyrin Dimers Bridged by Aromatic Linkers. *Eur. J. Inorg. Chem.* **2007**, *2007*, 1844−1853.
(104) Rondon, S.; Sherwood, P. M. Core Level and Valence Band Spectra of PbO by XPS. *Surf. Sci. Spectra* **1998**, *5*, 97−103.
(105) Crist, B. V. *Handbook of Monochromatic XPS Spectra*; Wiley: 2000.
(106) Baltrusaitis, J.; Chen, H.; Rubasinghege, G.; Grassian, V. H. Heterogeneous Atmospheric Chemistry of Lead Oxide Particles with Nitrogen Dioxide Increases Lead Solubility: Environmental and Health Implications. *Environ. Sci. Technol.* **2012**, *46*, 12806−12813.
(107) Coleman, E. J.; Chowdhury, M. H.; Co, A. C. Insights Into the Oxygen Reduction Reaction Activity of Pt/C and PtCu/C Catalysts. *ACS Catal.* **2015**, *5*, 1245−1253.
(108) Pourbaix, M. *Atlas of Electrochemical Equilibria in Aqueous Solutions*; National Association of Corrosion Engineers: 1974.
(109) Dekel, D. R.; Amar, M.; Willdorf, S.; Kosa, M.; Dhara, S.; Diesendruck, C. E. Effect of Water on the Stability of Quaternary Ammonium Groups for Anion Exchange Membrane Fuel Cell Applications. *Chem. Mater.* **2017**, *29*, 4425−4431.
(110) Zitolo, A.; Goellner, V.; Armel, V.; Sougrati, M.-T.; Mineva, T.; Stievano, L.; Fonda, E.; Jaouen, F. Identification of Catalytic Sites for Oxygen Reduction in Iron- and Nitrogen-Doped Graphene Materials. *Nat. Mater.* **2015**, *14*, 937.
(111) Lefèvre, M.; Dodelet, J.-P. Fe-Based Catalysts for the Reduction of Oxygen in Polymer Electrolyte Membrane Fuel Cell Conditions: Determination of the Amount of Peroxide Released during Electroreduction and Its Influence on the Stability of the Catalysts. *Electrochim. Acta* **2003**, *48*, 2749−2760.
(112) Chu, W.; Higgins, D.; Chen, Z.; Cai, R. Non-Precious Metal Oxides and Metal Carbides for ORR in Alkaline-Based Fuel Cells. In *Non-Noble Metal Fuel Cell Catalysts*; Chen, Z., Dodelet, J.-P., Zhang, J., Eds.; Wiley-VCH Verlag GmbH & Co. KGaA: 2014; pp 357−388.
(113) Thorseth, M. A.; Tornow, C. E.; Tse, E. C. M.; Gewirth, A. A. Cu Complexes That Catalyze the Oxygen Reduction Reaction. *Coord. Chem. Rev.* **2013**, *257*, 130−139.
(114) Vazquez, M. V.; de Sanchez, S. R.; Calvo, E. J.; Schiffrin, D. J. The Electrochemical Reduction of Oxygen on Polycrystalline Copper in Borax Buffer. *J. Electroanal. Chem.* **1994**, *374*, 189−197.
(115) Liu, K.; Song, Y.; Chen, S. Electrocatalytic Activities of Alkyne-Functionalized Copper Nanoparticles in Oxygen Reduction in Alkaline Media. *J. Power Sources* **2014**, *268*, 469−475.

DOI: 10.1021/acscatal.8b01045
ACS Catal. 2018, 8, 8618−8629

(116) Goubert-Renaudin, S. N. S.; Wieckowski, A. Ni and/or Co Nanoparticles as Catalysts for Oxygen Reduction Reaction (ORR) at Room Temperature. *J. Electroanal. Chem.* **2011**, *652*, 44−51.
(117) Levy, N.; Mahammed, A.; Kosa, M.; Major, D. T.; Gross, Z.; Elbaz, L. Metallocorroles as Nonprecious-Metal Catalysts for Oxygen Reduction. *Angew. Chem., Int. Ed.* **2015**, *54*, 14080−14084.
(118) El-Nagar, G. A.; Derr, I.; Fetyan, A.; Roth, C. One-Pot Synthesis of a High Performance Chitosan-Nickel Oxyhydroxide Nanocomposite for Glucose Fuel Cell and Electro-Sensing Applications. *Appl. Catal., B* **2017**, *204*, 185−199.
(119) Wu, K.-H.; Allen-Ankins, M.; Zeng, Q.; Zhang, B.; Pan, J.; Zhang, J.; Su, D.-S.; Gentle, I. R.; Wang, D.-W. Benchmarking the Oxygen Reduction Electroactivity of First-Row Transition-Metal Oxide Clusters on Carbon Nanotubes. *ChemElectroChem* **2018**, *5*, 1862−1867.
(120) Noori, M. T.; Ghangrekar, M. M.; Mukherjee, C. K. V_2O_5 Microflower Decorated Cathode for Enhancing Power Generation in Air-Cathode Microbial Fuel Cell Treating Fish Market Wastewater. *Int. J. Hydrogen Energy* **2016**, *41*, 3638−3645.
(121) Liu, Z.; Anson, F. C. Electrochemical Properties of Vanadium(III,IV,V)−Salen Complexes in Acetonitrile. Four-Electron Reduction of O_2 by V(III)−Salen. *Inorg. Chem.* **2000**, *39*, 274−280.
(122) Wen, C.; Gao, X.; Huang, T.; Wu, X.; Xu, L.; Yu, J.; Zhang, H.; Zhang, Z.; Han, J.; Ren, H. Reduced Graphene Oxide Supported Chromium Oxide Hybrid as High Efficient Catalyst for Oxygen Reduction Reaction. *Int. J. Hydrogen Energy* **2016**, *41*, 11099−11107.
(123) Zagal, J. H.; Koper, M. T. M. Reactivity Descriptors for the Activity of Molecular MN_4 Catalysts for the Oxygen Reduction Reaction. *Angew. Chem., Int. Ed.* **2016**, *55*, 14510−14521.
(124) Coowar, F.; Contamin, O.; Savy, M.; Scarbeck, G.; van den Ham, D.; Riga, J.; Verbist, J. J. Investigation of O_2 Reduction in Alkaline Media on Supported Mo Naphthalocyanines: Effect of the Support and of the Isomer Configuration. *J. Electroanal. Chem. Interfacial Electrochem.* **1989**, *269*, 143−162.
(125) Prestat, M.; Vucko, F.; Lescop, B.; Rioual, S.; Peltier, F.; Thierry, D. Oxygen Reduction at Electrodeposited ZnO Layers in Alkaline Solution. *Electrochim. Acta* **2016**, *218*, 228−236.
(126) Türk, K.-K.; Kaare, K.; Kruusenberg, I.; Merisalu, M.; Joost, U.; Matisen, L.; Sammelselg, V.; Zagal, J. H.; Tammeveski, K. Oxygen Electroreduction on Zinc and Dilithium Phthalocyanine Modified Multiwalled Carbon Nanotubes in Alkaline Media. *J. Electrochem. Soc.* **2017**, *164*, H338−H344.
(127) Slot, T. K.; Eisenberg, D.; Rothenberg, G. Cooperative Surface-Particle Catalysis: The Role of the "Active Doughnut" in Catalytic Oxidation. *ChemCatChem* **2018**, *10*, 2119−2124.

DOI: 10.1021/acscatal.8b01045
ACS Catal. 2018, 8, 8618−8629